Microstructure of Polycrystalline PBTTT Films: Domain Mapping and Structure Formation

Torben Schuettfort,[†] Benjamin Watts,[§] Lars Thomsen,[⊥] Mijung Lee,[‡] Henning Sirringhaus,[†] and Christopher R. McNeill[||],*

[†]Cavendish Laboratory, University of Cambridge, J. J. Thomson Avenue, Cambridge, CB3 0HE, United Kingdom, [‡]School of Advanced Materials Engineering, Kookmin University, University, 861-1 Jeongneung-dong, Seongbuk-gu, Seoul 136-702, Korea, [§]Paul Scherrer Institut, 5232 Villigen PSI, Switzerland, [⊥]The Australian Synchrotron, 800 Blackburn Road, Clayton, Victoria 3168, Australia, and [||]Department of Materials Engineering, Monash University, Clayton, Victoria 3800, Australia

The performance of solution-processable conjugated polymers has risen significantly over the past two decades and now matches the performance of amorphous silicon.[1] This enables deployment in electronic devices such as organic field-effect transistors (OFETs) for display or logic applications.[2] The increasing library of materials with high charge mobilities combined with improvements in materials stability and device engineering are bringing conjugated polymers closer to realize their potential for low-cost flexible electronics. High hole mobilities were observed in the polymer poly(3-hexylthiophene) (P3HT) over a decade ago, with large variations in mobility for different deposition conditions that alter the microstructure of the films.[3] The liquid crystalline polymer poly(2,5-(3-alkylthiophen-2-yl)thieno[3,2-b]thiophene) (PBTTT) allows better control of the microstructure through interdigitation of the side chains, which produces more consistent charge mobilities.[4]

A central issue in understanding the functionality of these new materials is the relationship between film microstructure and charge transport.[5,6] Many high-mobility polymers exhibit semicrystalline order, although the absolute degree of crystallinity for most of these materials and the influence of crystallinity on device functionality are not fully known. Instrumental to the study of structure/function relationships in semiconducting polymers is the ability to assess film microstructure as relevant to device performance. Grain boundaries in polycrystalline materials have long been suspected as being transport barriers in OFETs. While for solution-processed small molecule devices it has been shown that also the nature of the grain boundary has strong impact on the device

ABSTRACT
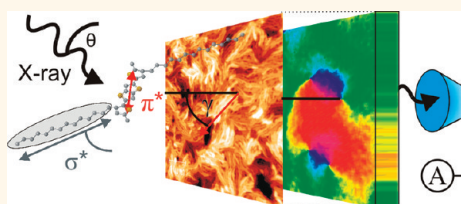
We utilize near-edge X-ray absorption fine structure (NEXAFS) spectroscopy and scanning transmission X-ray microscopy (STXM) to study the microstructure and domain structure of polycrystalline films of the semiconducting polymer poly(2,5-bis(3-tetradecylthiophen-2-yl)thieno-[3,2-b]thiophene) (PBTTT). Total electron yield NEXAFS spectroscopy is used to examine the surface structure of the first 1—2 molecular layers, while bulk-sensitive STXM is used to produce maps of domain orientation and order sampled through the entire film thickness. We study different phases of PBTTT including as-cast, terraced and nanoribbon morphologies produced via spin-coating as well as aligned films of as-cast and nanoribbon morphologies produced by zone-casting. For the terraced morphology, domains are observed that are larger than the size of the terraced surface features, and the calculated degree of order is reduced compared to the nanoribbon morphology. For zone-cast films, we find that, although little optical anisotropy is observed in the bulk of as-cast films, a high degree of surface structural anisotropy is observed with NEXAFS spectroscopy, similar to what is observed in annealed nanoribbon films. This observation indicates that the aligned surface structure in unannealed zone-cast films templates the bulk ordering of the aligned nanoribbon phase. STXM domain mapping of aligned nanoribbon films reveals elongated, micrometer-wide domains with each domain misoriented with respect to its neighbor by up to 45°, but with broad domain boundaries. Within each nanoribbon domain, a high degree of X-ray dichroism is observed, indicating correlated ordering throughout the bulk of the film.

performance,[7] similar measurements are more challenging in semiconducting polymers due to the much smaller domain sizes of the coherent crystallites.

Despite the perceived importance of domain structure in polycrystalline polymer films, it has only been in recent years that experimental techniques have been employed to image semicrystalline domain

structure.[8] While conventional cross-polarized optical microscopy is suitable for the study of domains on the length scale of micrometers or more,[7] more sophisticated techniques are required to examine domain structure on the submicrometer length scale. A number of approaches have been successful at probing the domain structure on this length scale including scanning probe-based transverse shear microscopy,[9,10] dark-field electron microscopy,[11,12] near-field scanning optical microscopy,[13] and scanning transmission X-ray microscopy.[14−17]

The structure of PBTTT films is perhaps the best understood of all semiconducting polymers owing to its relatively high crystallinity.[18] X-ray diffraction (XRD) studies have shown that in-plane $\pi-\pi$ stacking and out-of-plane lamellae ordering are found even in films not subjected to heat treatment.[19] PBTTT also exhibits a number of characteristic thin-film morphologies including the so-called terraced and nanoribbon morphologies. The terraced morphology is produced after heating the film above the first thermal transition (corresponding to melting of the alkyl side chains[20]) and cooling to room temperature. The topography exhibits the characteristic, wide, molecular-height terraces that are readily observable by atomic force microscopy (AFM).[4] The nanoribbon morphology is accessed after heating above the second phase transition (likely associated with backbone melting[21]) and cooling to room temperature and is characterized by the formation of nanoribbons of fully extended polymer chains.[21] Alignment of these nanoribbons is also possible through directional deposition processes such as flow-coating or zone-casting.[21,22] In the zone-casting process, the polymer solution is deposited onto a moving, heated substrate which produces aligned polymer backbones following the direction of solidification during solution coating.

The high crystallinity of PBTTT has allowed for modeling of the unit cell based on XRD data, which is generally not possible for conjugated polymers due to the disorder present in solution-processed films.[23] These calculations are also in agreement with near-edge X-ray absorption fine structure (NEXAFS) measurements of the backbone and side chain tilt angles at the top surface of PBTTT films.[24] However, a recent thorough analysis of XRD reveals that the degree of paracrystalline disorder in the $\pi-\pi$ stacking direction is high even in this highly crystalline semiconducting polymer system.[25] Although micrometer-sized topographic features are observed in the terraced or ribbon morphologies, XRD and transmission electron microscopy (TEM) work has shown that in-plane coherent ordering in these films is likely to be on much smaller length scales of ∼7 nm.[21,26] It is therefore important to distinguish between coherent crystalline domains and quasi-domains of parallel backbones which are imaged in this work. A detailed analysis of the field-effect
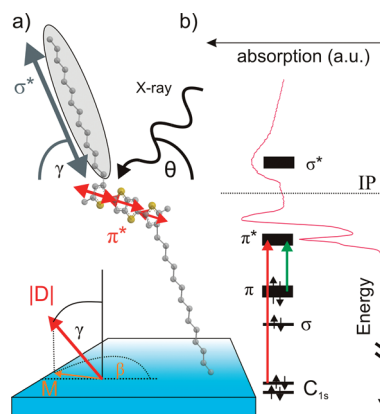

Figure 1. (a) Molecular drawing of a PBTTT monomer with the NEXAFS transition dipole moments (TDMs) and the relevant angles for the X-ray angle of incidence (θ) and molecular orientation (γ) measured with respect to the substrate. The in-plane component M of the total TDM resonance $|D|$ is drawn in orange with its in-plane orientation β. **(b)** Arbitrary molecular energy levels for a π-conjugated system with the NEXAFS spectrum arising due to transitions from the C1s to the antibonding molecular orbitals (an optical transition is shown in green for reference) and above the ionization potential (IP).

mobility anisotropy in aligned PBTTT films also stressed that the nature of the quasi-domain boundaries seems to influence the overall mobility,[27] similar to the observations made for aligned P3HT films.[28] In isotropic nanoribbon PBTTT films, scanning Kelvin probe microscopy has shown that charge trapping in this particular morphology seems to predominantly occur at the edges of ribbons, indicating that these quasi-domains may be most influential in determining the average mobility.[29] The good charge transport properties and the rich microstructure of PBTTT thus make it an excellent material for the study of structure/function relationships.

In this contribution, we utilize NEXAFS spectroscopy and STXM to study the domain structure of the various PBTTT morphologies and present mechanisms for structure formation. In the first part of the article, we analyze surface-sensitive NEXAFS spectra of zone-cast and spin-coated films as-deposited as well as after annealing into the terraced and nanoribbon morphologies. We then characterize the bulk morphology of the entire film thickness by taking STXM images with high lateral resolution: For the terraced morphology, we obtain similar domain orientation maps as previously presented by Zhang et al. using a dark-field transmission electron microscopy (DF-TEM) technique[12] but with higher angular resolution. We extend this work to map the domain orientation of isotropic and aligned nanoribbons. Furthermore, using our approach to map the local molecular order (previously used for the study of polycrystalline poly(9,9′-dioctyl-fluorene-co-benzothiadiazole) films[16]), we reveal new information about the quasi-domain structure and molecular ordering in PBTTT films. Finally, we show

a) As Spun

b) As Zone Cast

c) Terraced

d) Height distribution:

e) Isotropic nano-ribbon
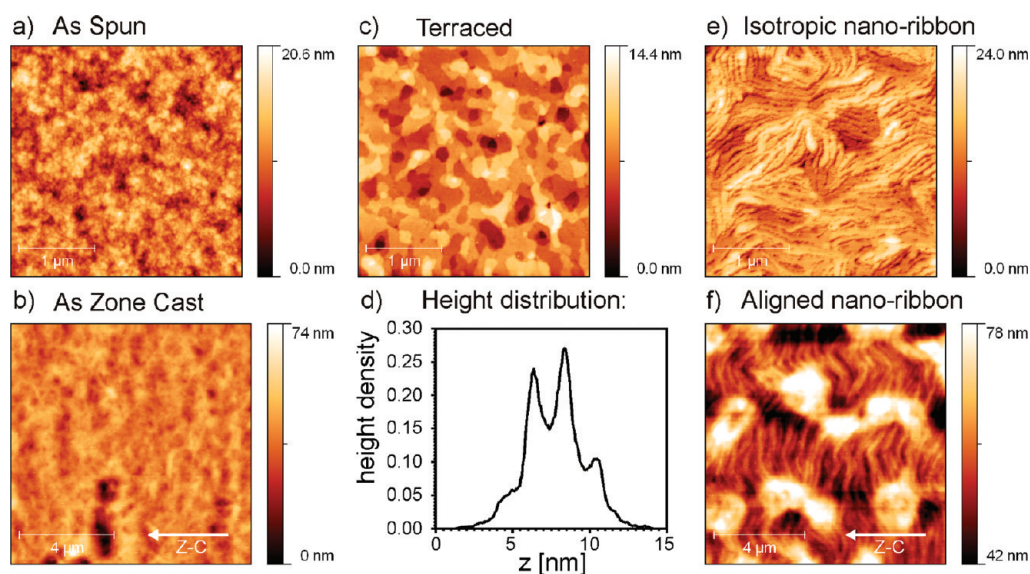
f) Aligned nano-ribbon

Figure 2. AFM topography images of the as-prepared spin-coated (a) and zone-cast (b) sample with the zone-casting (Z-C) direction as drawn. (c) Topography of the terraced morphology accessed after annealing. The height distribution histogram of this terraced sample is shown in (d), yielding a step height of ∼1.9 nm. The topography images of the nanoribbon morphology after annealing a spin-coated sample (e) and a zone-cast sample (f).

that during the deposition of zone-cast PBTTT films a high degree of surface alignment is produced that templates bulk ordering during thermal treatment.

RESULTS AND DISCUSSION

In the following, we characterize the morphology of PBTTT thin films both deposited by spin-coating as well as zone-casting.[21] A molecular drawing of the chemical structure of a PBTTT monomer is shown in Figure 1a together with its the NEXAFS transition dipole moments (TDMs). To characterize the molecular ordering at the surface of films, we have utilized angle-resolved NEXAFS spectroscopy. In this experiment, soft X-rays are used to probe resonant transitions from the carbon 1s orbital into unoccupied molecular orbitals. Figure 1b shows an arbitrary NEXAFS spectrum arising from transitions into different unoccupied molecular states.

Isotropic PBTTT samples produced *via* spin-coating on a bare silicon wafer with a native oxide were measured as-spun and annealed into the terraced and isotropic nanoribbon phases. AFM images of these morphologies are shown in Figure 2a,c. As reported previously, the as-spun sample has no apparent topographical features, while the terraced morphology exhibits ∼1.9 nm molecular steps of in-plane π-stacked backbone layers separated by their interdigitating side chains (see Figure 2d).[30] After annealing above the second phase transition temperature, the isotropic nanoribbons are formed, featuring ribbons with a width of about one extended polymer chain ∼60 nm, as seen in Figure 2e (for height distribution, see Supporting Information).[21] The NEXAFS spectra of all samples are fairly similar to the spectrum of terraced PBTTT shown in Figure 3a. The resonances as

previously identified are the C1s → π^* transition around 285 eV, the C1s → σ^* of the carbon−hydrogen and carbon−sulfur bonds at 287.1 eV, and the carbon−carbon C1s → σ^* at 293.1 eV.[24]

Due to the localized nature of the C1s orbital, analysis of the different NEXAFS resonances allows assessment of the orientation of different parts of the molecular structure. As shown in Figure 1b, the C1s → π^* TDM (shown in red) is only found on the conjugated backbone perpendicular to the ring planes.[24,31] The C1s → σ^* TDM, which is oriented parallel to the σ bonds, is predominantly found in the C-14 alkyl chains (gray). However, the measurement is of the ensemble of transition dipole moments (TDMs) within the sample, and the extracted molecular orientation represents the average orientation. In order to accurately extract the dichroism for an observed transition, we utilized peak fitting of the observed resonances. Peak positions were identified using difference spectra, and Gaussian peaks were used to fit molecular resonances and a step function to fit the ionization potential (plotted in the Supporting Information). For PBTTT, we examine two peaks in the π^* region at 284.5 and 285.1 eV as well as a σ^* peak at 293.1 eV.

To measure the dichroism of the TDMs, the X-ray angle of incidence, θ, onto a thin-film sample is varied. A NEXAFS absorption event produces Auger electrons from the core-excited carbon atoms. On the way to the surface, these produce secondary electrons through scattering, which can be used as a measure for NEXAFS spectra with a probing depth of ∼2.5 nm.[32,33] The surface-sensitive NEXAFS spectra of the terraced PBTTT sample shown in Figure 3a were recorded at incident angles of θ = 20, 40, 55, 70, and 90°, and
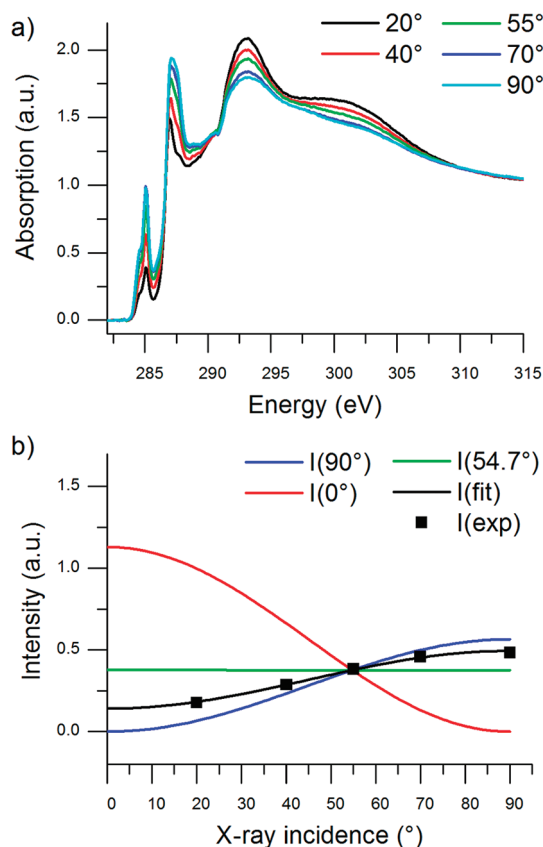
Figure 3. (a) Terraced PBTTT NEXAFS spectra for different X-ray angles of incidence as defined in Figure 1a. **(b)** Peak heights of the $1s \rightarrow \pi_1^*$ transition are plotted as a function of θ and fitted to the theoretical function, eq 2, to extract the tilt angle of the TDM. Also shown in part (b) are theoretical peak height *vs* θ plots for molecules oriented with the polymer backbone perfectly flat ($\gamma = 0°$), perfectly edge-on ($\gamma = 90°$), or oriented at the so-called "magic angle" ($\gamma = 54.7°$).

pronounced dichroism of the resonance peaks is observed. Equation 2 was then used to calculate the average tilt angle of the π^* and C−C σ^* TDM with respect to the substrate plane, as shown in Figure 3b. Two Gaussian peaks were fitted to the π^* region of the spectrum, and tilt angles of both π^* peaks were analyzed individually. Although theoretically both angles should be equal, their spread provides information regarding the uncertainty of the measured tilt angles. Since the ring-plane of the conjugated backbone is perpendicular to the π^* TDM, the angle between the backbone plane and the surface normal may be calculated as $90° - \gamma$ (see Figure 1). All calculated values for γ are between 63 and 72°, indicating a pronounced edge-on character of the polymer backbone, with slightly lower γ values found for the isotropic nanoribbon sample. It is important to note that these values are to be understood as the average of a distribution of molecular tilt angles, even though the values are far away from the "magic" angle 54.7°,[31] which could represent an entirely amorphous sample as well as a narrow distribution around 54.7°. The actual distribution
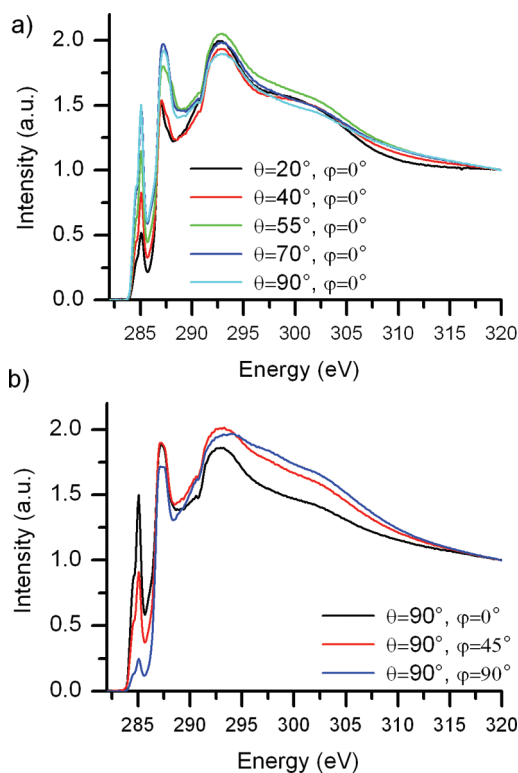

Figure 4. NEXAFS spectra of the aligned nanoribbon sample. The X-ray angle of incidence dependence is shown in (a) for an in-plane azimuth angle of $\varphi = 0°$, while the φ dependence is shown in (b) for an X-ray angle of incidence of $\theta = 90°$. Both measurements show strong dichroism.

of tilt angles cannot be measured using the surface NEXAFS scans but can be calculated from bulk scans as discussed below. Since the majority of the σ^* TDM is found on the side chains as opposed to the backbone, the tilt angle of this TDM can be seen as a measure of the tilt angle of the side chains. The calculated value is very similar for all samples at around 45°, which is again sufficiently away from the magic angle.

Since the fitting results for all spin-coated samples are very similar to each other and in good agreement with results published previously for the terraced morphology,[24] we can conclude that the molecular orientation at the surface is very similar for all samples despite the large differences observed in the topography in Figure 2a,c,e for the as-spun, terraced, and isotropic nanoribbon samples, respectively. The fact that the rather amorphous topography of the as-spun PBTTT film revealed by AFM (compared to the extended terraces of the annealed film) exhibits pronounced dichroism highlights the weakness of AFM for providing information regarding film microstructure and the importance of X-ray characterization methods. Crystallites have also been observed to be present in both the terraced and as-spun morphologies with bulk-sensitive X-ray scattering, but with smaller and slightly less oriented crystallites with respect to the substrate for the latter morphology.[5,19]

TABLE 1. Measured Tilt Angle γ of the $\pi*$ TDM and Side Chains (C—C $\sigma*$ TDM) of the Spin-Coated (Isotropic) and Zone-Cast (Aligned) PBTTT Samples (the Latter Measured at an Azimuthal Angle of $\varphi = 0°$)

	transition		
sample	π_1* 284.5 eV	π_2* 285.1 eV	$\sigma*$ 293.1 eV
terraced PEY (ref 22)	$90° - 21° = 69°$		45°
as-spun (isotropic)	67°	67°	44°
terraced (this study)	69°	68°	44°
isotropic nanoribbon	66°	63°	45°
as-zone-cast	72°	71°	(44°)
aligned nanoribbon	67°	64°	(44°)

A similar picture is seen for the aligned films deposited by zone-casting. In these samples, the polymer backbone is aligned parallel to the zone-casting direction by means of directed solidification of the solution during deposition. The as-zone-cast morphology does not exhibit any apparent topological features, as shown in Figure 2b, similar to its isotropic counterpart. After annealing through the second phase transition, the characteristic aligned nanoribbons are formed as previously reported[21] and seen in the topography image in Figure 2f. In order to account for the loss of rotational symmetry in the samples, the NEXAFS spectra have to be measured as a function of the in-plane azimuth angle φ. Figure 4 presents NEXAFS spectra of the aligned nanoribbon sample as a function of X-ray angle of incidence, θ (at $\varphi = 0°$), and as a function of the in-plane azimuth angle, φ (for $\theta = 90°$) (see Supporting Information for as-zone-cast). When rotating the sample at normal X-ray incidence, a significant change in the $\pi*$ absorption intensity is observed. Strong absorption is observed for $\varphi = 0°$ and $\theta = 90°$ corresponding to the X-ray polarization being perpendicular to the zone-casting direction, as expected for polymer backbones aligned in the zone-casting direction. These spectra are similar to the spectra presented previously for an aligned nanoribbon film.[5] While the pronounced dichroism of the $\pi*$ absorption indicates strong backbone alignment, only small dichroism is observed in the $\sigma*$ transition when varying the X-ray angle of incidence θ or when rotating φ. For further analysis, it is possible to calculate the tilt angle γ from scans with varied θ using eq 3, and the results are also presented in Table 1. For $\varphi = 0°$, the backbone tilt angles calculated from the π_1* and π_2* peaks are again similar to those found for the isotropic samples, as shown in Table 1. It is interesting to note that the fitted values for the side chains $\sigma*$ are again close to 45°. When fitting the tilt angles using eq 3 for aligned samples, this angle represents the magic angle, where a completely random distribution of the TDMs is possible. However, since the same angle was extracted for the isotropic samples, where the consistent value of 45° is significantly away from the magic angle of 54.7° (for isotropic

samples), it is likely that the tilt angle of the side chains is indeed close to 45°. Since the dichroism is small upon rotation around φ, a preferential direction of the 45° tilted side chains with respect to the zone-casting direction cannot be extracted.

It is important to mention that the $\pi*$ absorption does not go to zero upon rotation around φ but keeps a constant background value independent of the X-ray angle of incidence. According to eq 3, no matter what value is found for the tilt γ of the $\pi*$ TDM, the $\pi*$ absorption should always go to zero for $\theta = \varphi = 90°$ for perfectly aligned polymer chains (when using the undulator photon source with a polarization ratio $P \approx 1$). We therefore attribute this significant absorption to a substantial misalignment of the polymer backbones from the zone-casting direction. This misalignment is confirmed by the STXM images in the form of elongated domains with backbone direction diverging from the zone-cast direction as shown and discussed in detail below.

The surface-sensitive NEXAFS spectra can also be used to provide insight into the ordering mechanism of the zone-casting process. For both the aligned nanoribbon (Figure 4) and the as-zone-cast sample, pronounced dichroism is observed in the surface NEXAFS spectra upon rotation around φ, as shown in Figure 5b in the $\pi*$ region of the spectra (full spectra in Figure 4 and Supporting Information). However, this is not observed in optical anisotropy measurements in Figure 5a which probe the $\pi-\pi*$ absorption throughout the bulk of a film (inclusive of the film surface). This $\pi-\pi*$ TDM is parallel to the backbone in thiophene polymers, and optical anisotropy measurements have been used previously in order to establish the degree of alignment of PBTTT films.[21] As shown in Figure 5a, the optical anisotropy is significantly lower in the as-zone-cast film, indicating that the degree of backbone alignment in the bulk is inferior to the aligned nanoribbon morphology, in agreement with previous measurements.[21,27] The optical and X-ray anisotropy can be quantified as a measure for backbone alignment in the bulk and at the surface, respectively, using the expression

$$D = \frac{A_{\parallel} - A_{\perp}}{A_{\parallel} + A_{\perp}} \qquad (1)$$

The values of D_{bulk} presented in Table 2 are calculated at the maximum of the absorbance at 2.3 eV, where D_{bulk} takes on its largest value in the spectrum. The value of D_{bulk} derived for the as-zone-cast sample is significantly lower than for the aligned nanoribbon sample. On the other hand, the dichroism values of the surface-sensitive NEXAFS spectra calculated using eq 1 are almost equal with $D_{surf} = 0.72$ and $D_{surf} = 0.73$ for the as-zone-cast and aligned nanoribbon samples, respectively, at 285.1 eV (the energy where the largest dichroism is found). Furthermore, the values for D_{surf}
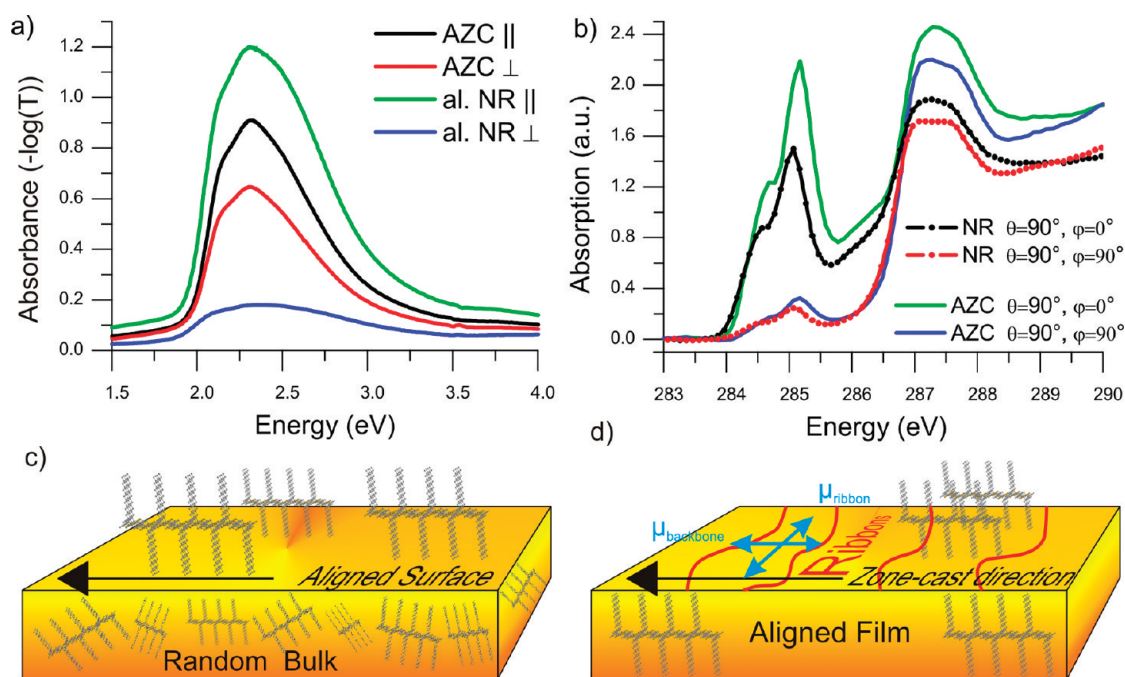
Figure 5. (a) Optical (bulk) absorption of the as-zone-cast (AZC) and aligned nanoribbon (al. NR) sample with polarization parallel and perpendicular to the zone-cast direction (data from ref 27). Bulk dichroism of the as-zone-cast sample is significantly reduced compared to the aligned nanoribbon sample. (b) NEXAFS (surface) spectra at normal X-ray angle of incidence ($\theta = 90°$). The ordering mechanism is drawn in (c) and (d), where the as-zone-cast sample in (c) is predominantly aligned at the surface with randomly oriented crystallites and amorphous chains in the bulk, while the aligned nanoribbon sample in (d) is aligned throughout the bulk.

TABLE 2. Values of the Optical (D_{bulk}) and NEXAFS (D_{surf}) Dichroism and the Mobility in Chain ($\mu_{backbone}$) and $\pi-\pi$ Stacking ($\mu_{\pi-\pi}$) Direction (Perpendicular to the Backbone and Parallel to the Ribbons in the Aligned Nanoribbon Sample; Given in [cm^2 (Vs)$^{-1}$])^a

sample	D_{surf}	D_{bulk}	$\mu_{\pi-\pi}$	$\mu_{backbone}$
as-zone-cast	0.72	0.17	0.036	0.29
aligned NR	0.73	0.74	0.088	0.36

^{a} It is clear that, for the as-zone-cast sample, the optical dichroism is significantly lower compared to the aligned nanoribbon film, while the NEXAFS dichroism and the backbone mobility values at this surface are similar in the as zone-cast and aligned nanoribbon sample.

are almost equal to the value found in the bulk of the aligned nanoribbon sample. This observation indicates that the same amount of alignment is present at the surface directly after zone-casting and after annealing. When assuming the same probing depth for the PBTTT total electron yield (TEY) spectra as previously determined for P3HT at ~2.5 nm,[32] one would expect an optical dichroism of $D_{bulk} = D_{surf}(2.5 \text{ nm}/70 \text{ nm}) = 0.036$ for the 70 nm thick zone-cast film if all aligned polymer chains were within the NEXAFS probing depth and there was no further alignment in the bulk. However, the measured value $D_{bulk} = 0.17$ for the entire film thickness is larger, which indicates that aligned polymer backbones are not found exclusively at the top surface but also buried deeper in the film than the probing depth of the TEY measurement. From this

analysis, we conclude that the alignment of polymer chains is formed predominantly at the surface of the PBTTT films during zone-casting and templates the bulk ordering during annealing as sketched in Figure 5. We speculate that the alignment of polymer chains is decreasing from the surface into the film. In an earlier publication, where aligned PBTTT films were prepared using a flow-coating technique that is conceptually similar to the zone-casting technique employed here, the alignment mechanism was not entirely clear.[20] Our measurements show that the alignment is produced at the top surface of the film, probably due to the shear force exerted by the bar onto the film surface or the curvature of the solution/air interface during solvent evaporation.

The surface alignment on the as-zone-cast film is further confirmed by mobility anisotropy measurements in top-gate bottom contact OFETs shown in Figure 6. In this transistor geometry, charge accumulation occurs at the top surface of the PBTTT film, the same surface that is probed with NEXAFS spectroscopy prior to deposition of the gate dielectric. When the saturation mobility is measured perpendicular and parallel to the polymer backbone direction in aligned nanoribbon films, significant mobility anisotropy is observed as presented previously for bottom-gate OFETs.[27] In the top-gate structure, the mobility parallel to the backbone direction is very similar with $\mu_{backbone} = 0.29 \text{ cm}^2/(\text{Vs})$ for the as zone-cast

a)

Aligned Nano-Ribbon
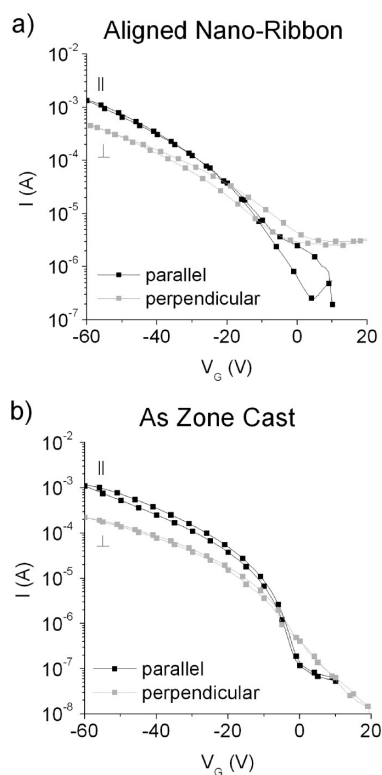

b)

As Zone Cast

Figure 6. Transfer curves of top-gated devices at a source–drain voltage of $V_{SD} = -60$ V measured perpendicular and parallel to the zone-casting direction for (a) the aligned nanoribbon and (b) the as zone-cast morphology.

and $\mu_{backbone} = 0.36$ cm^2/(Vs) for the aligned nanoribbon sample calculated from the transfer curves shown in Figure 6 and summarized in Table 2. This strongly supports our alignment model sketched in Figure 5: The same degree of backbone alignment at the surface of as-zone-cast and aligned nanoribbon films allows for efficient charge transport parallel to the backbones, despite less alignment being found in the bulk of as-zone-cast samples. For the as-zone-cast morphology, the charge mobility for transport along the $\pi-\pi$ stacking direction perpendicular to the aligned backbone, $\mu_{\pi-\pi} = 0.036$ cm^2/(Vs), is significantly lower than that of the aligned nanoribbon sample, $\mu_{\pi-\pi} = 0.088$ cm^2/(Vs). This difference in mobility along the $\pi-\pi$ stacking direction can be attributed to the presence of defects in the $\pi-\pi$ stacking, which are healed through ribbon formation.

A more detailed picture of the morphology of PBTTT films emerges when probing the NEXAFS absorbance locally. STXM has been extensively used to map the morphology of conjugated polymer blends for solar cell application as it allows for chemical sensitivity in blends at high resolutions.[8,34,35] The polarization of synchrotron radiation also allows local mapping of the dichroism of thin films, as shown for pentacene[15] and a high mobility electron transporting polymer.[36] For these measurements, we have recently presented a novel analysis method together with measurements

on poly(9,9′-dioctylfluorene-*co*-benzothiadiazole) (F8BT) to extract images detailing the local degree of order and local tilt angle γ of the π^* TDM.[16]

In order to investigate the long-range backbone orientation, we performed bulk-sensitive STXM measurements which probe the entire film thickness. After annealing, the spin-coated and zone-cast samples exhibit strong local dichroism of the 1s–π^* transition, which is inverted upon polarization rotation (see Supporting Information). The locally resolved backbone orientation of PBTTT thin films is calculated using eq 4 from STXM images recorded with rotated in-plane polarization (0, 45, 90, and 135°). When comparing the AFM image shown in Figure 7a and the backbone orientation map (b) of the terraced morphology, it becomes clear that domains of parallel backbones are larger than the average size of the topological terraces. Note that the AFM image was taken at a different position of the same film, while the property maps calculated from STXM all correspond to the same location. The fact that domains of parallel backbones are observed means that out-of-plane registry between terraced layers within the film exists for parallel backbone alignment of adjacent layers. This is expected for PBTTT due to the side chain interdigitation which is generally thought to promote the ordering of the material.[30] Similar maps of the backbone orientation have been calculated from DF-TEM images by Zhang *et al.* for terraced PBTTT.[12] Despite the higher resolution of this electron scattering approach (3.8 nm pixel size), the quality of the orientation maps is limited due to experimental artifacts such as arcing of the diffraction peaks, which could indicate multiple crystallite orientations, as well as the presence of other scattering peaks and diffuse backgrounds, which may contribute to the signal in the aperture. Therefore, these high-resolution DF-TEM measurements can only distinguish eight angular orientations of the crystallites. Even though the STXM approach only measures four angles of incidence of the polarization, the precise angle of the TDM ensemble can be fitted using eq 4 due to the well-known cos^2 relationship of the resonance intensity to the angle between the X-ray polarization and the TDM. It is also important to emphasize that in this approach only the ordered polymer backbones are included in the backbone orientation map, as only the in-plane magnitude of the directed resonance intensity (parameter M in eq 4 as depicted in orange in Figure 1a) is oriented at the plotted angle β. The isotropic contribution extracted from the fit can be used to calculate the degree of order as discussed below. Furthermore, STXM measurements allow for direct thickness normalization by simply imaging at an energy that is not in resonance with any dichroic transitions. In the DF-TEM study, the authors observed speckles ~20 nm in size within the quasi-domains of parallel backbones, which were related to coherent
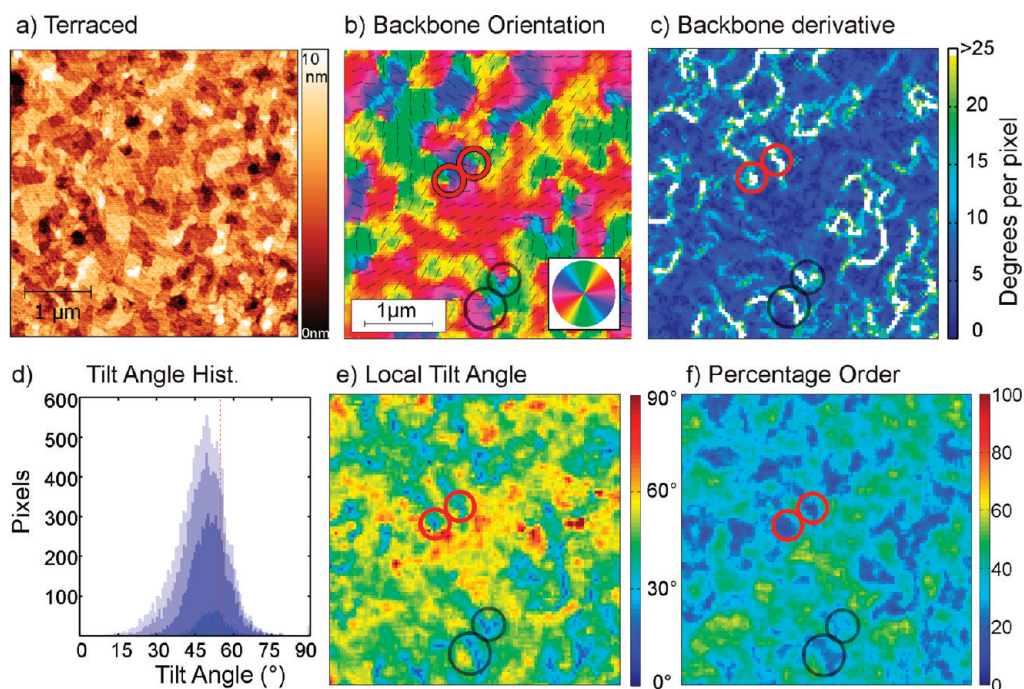
Figure 7. (a) AFM image of terraced PBTTT on mica substrate before floating off for X-ray transmission measurements. (b) Backbone orientation map calculated from multiple STXM images taken of the same spot of the film but with different incident linear polarization of the X-ray beam, (c) the rate of change of the backbone orientation, (e) the local tilt angle map, and (f) the % order. (d) Details the histogram of the local tilt angle map by including all pixels (light blue), pixels with >25% order, >33% order, and >45% order (dark blue). Two nearby pairs of half integer disclinations are circled in red and black in (b), (c), (e), and (f) (two disclinations in each circle).

crystalline domains. In fact, the diffraction method is only sensitive to coherent crystals, while the STXM measurements presented here probe the ensemble of C1s $\rightarrow \pi^*$ TDMs within any given pixel and is therefore sensitive to the degree of orientational order of aligned backbones as discussed in detail below. The backbone orientation map for PBTTT exhibits the characteristics of a nematic liquid crystal, with half integer disclinations with opposite signs found in pairs similar to previous observation.[12] Furthermore, two pairs of half integer disclinations are often found in close vicinity, with the same sign found at opposite corners of the formed square.

It has often been discussed that large angle grain boundaries may have a greater impact on the charge transport performance compared to low-angle boundaries.[12] In order to illustrate the presence of large angle boundaries of the domains of parallel backbones, we calculate the rate of change of the polymer backbone per pixel as drawn in Figure 7c. There is a clear population of "high-angle" boundaries with >25° change in orientation per pixel, but these rarely enclose areas within the film, so that percolation paths may exist around these barriers. These quasi-domain boundaries are rarely more than two pixels (80 nm) wide, which is the resolution limit for this sample. Interestingly, the backbone derivative map also reveals substructure that is not apparent in the backbone orientation image. Specifically, texturing is

observed within quasi-domains in addition to the high-angle domain boundaries mentioned above.

The local degree of order can be calculated using eq 8, which compares at any given pixel the strength of the directed TDM to the total resonance intensity (TRI), which originates from absorption processes averaged over all incoming X-ray polarizations (all assumptions are detailed in the Methods section). The calculated degree of order is therefore not a measure of the degree of crystallinity, but rather the degree to which the molecular moieties are oriented in the same direction, with no reference to their translational order. When comparing the backbone orientation map in Figure 7b to the percentage order map in (f), it is clear that the sites of half integer disclinations always correlate with sites of reduced order. Considering that a disclination by definition is a point where different backbone directions converge, this is in agreement with our understanding of the calculated order. Regions of reduced order are also found along high-angle domain boundaries. This highlights the advantage of using X-ray absorption characterization techniques over scattering and topography measurements to fully characterize the morphology of thin films.

The average degree of order for the terraced morphology in Figure 7f is only around $35 \pm 6\%$ (errors are estimated from a variation around TRI $= 2.4 \pm 0.2$; see Supporting Information), which is significantly lower than that of the semicrystalline F8BT previously
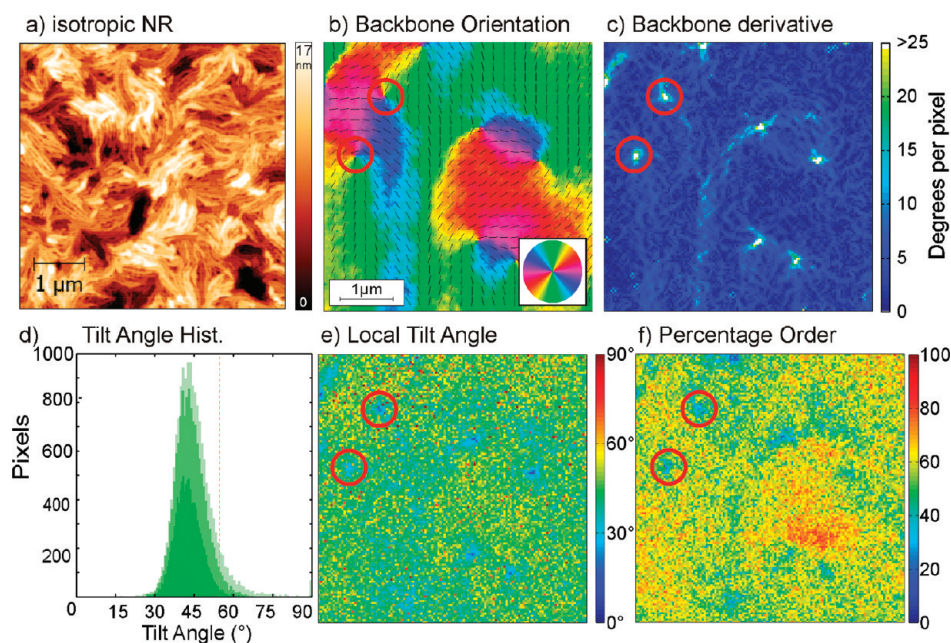
Figure 8. (a) AFM image of isotropic nanoribbon PBTTT on a mica substrate before floating off for X-ray transmission measurements. (b) Backbone orientation map calculated from multiple STXM images taken at the same spot of the film but with different incident linear polarization of the X-ray beam, (c) rate of change of the backbone orientation, and (f) degree of order map. The local tilt angle is shown in (e) and the corresponding histogram including all pixels (light green), pixels with >48% order, >54% order, and >65% order (dark green) in (d). The red circles in (b), (c), (e), and (f) indicate the locations of individual half integer disclinations.

investigated with this approach.[16] The low values of the degree of order could be due to the lack of interlayer registration of the polymer backbone direction. However, in an X-ray scattering study, it was found that even for quite thick (~70−100 nm) annealed PBTTT films the lamellae ordering extended all the way through the film thickness.[19] This is also in agreement with the DF-TEM results of terraced PBTTT, where for most of the pixels one predominant orientation was observed, although the scattering peaks exhibit arcing which could be related to a distribution of backbone orientations.[12] In the STXM data analysis, changes of the backbone orientation within the resolution of the experiment (~70 nm) also reduce the calculated degree of order. It is therefore reasonable to assume that the relatively low calculated order in the terraced films is not caused by lack of layer-to-layer registration of the backbone orientation but is predominantly caused by a large rate of change of the backbone orientation within a given pixel and between neighboring pixels. However, the degree of order distribution is fairly broad, and only within the largest quasi-domains the degree of order is in fact fairly large with values >60%. While we cannot assess the degree of order within the coherent crystallites, which is expected to be 100% because of the lamellae crystal structure, the long-range order is reduced due to the relatively small quasi-domains and areas of nonparallel backbones.

A slightly different trend is observed for the local tilt angle shown in Figure 7e. This angle is formed between the vectors M and D, as depicted in Figure 1a

and can be calculated using eq 9. The distribution of tilt angles shown in Figure 7d is rather broad, and the center is found around $47 \pm 12°$. This value is significantly different from the surface NEXAFS value of 68° found for terraced PBTTT as described above. This apparent inconsistency may be due to the fact that within the film the PBTTT backbone is actually tilted by an additional ~21° from the substrate normal. However, this is not in agreement with the unit cell calculations based on X-ray diffraction data of terraced PBTTT films[23] and X-ray scattering data that showed that lamellae crystallites extend all the way through the film thickness.[19] When comparing the tilt angle map (Figure 7e) to the degree of order map (Figure 7f), it can be seen that sites of reduced order such as the half integer disclinations correspond to lower tilt angle values. In fact, the calculated tilt angle histogram in Figure 7d shifts to higher values when considering only regions with a certain degree of order. For pixels with >60% order, which are found within the larger quasi-domains, the tilt angle approaches 54°. The tilt angle from eq 9 is calculated for the ordered transition dipole moment, which does not necessarily reflect coherent translational order probed by X-ray diffraction. The fact that the tilt angle in the bulk is reduced at sites of lower order could reflect that the oriented backbones, which are not necessarily crystalline, may have a reduced tilt angle compared to the crystals and the film surface. Since good agreement is found between the bulk and surface tilt angle for the aligned nanoribbon sample (vide infra), the lower value for the terraced sample may

indeed reflect a difference in molecular orientation between the bulk and the surface for this sample caused by aligned backbones that are not within coherent crystallites.

A slightly different picture emerges when analyzing the STXM images of the isotropic nanoribbon sample, summarized in Figure 8. Comparing the AFM image in Figure 8a to the backbone orientation map (b) (not taken at the same spot of the film) shows that the backbone direction follows the orientation of the ribbons as expected and that quasi-domains of parallel backbones consist of many parallel ribbons. In this morphology, the density of the nematic liquid crystalline half integer disclinations is much lower and the backbones are much more homogeneously aligned. We observe two clusters each with two pairs of half integer disclinations spaced much further apart compared to the terraced morphology shown in Figure 7b. It is again evident that the disclinations correspond to sites of low order in the order map Figure 8f. The backbone derivative map (Figure 8c) shows that in this sample there are regions with large change of backbone direction (>25° per pixel) only at the sites of disclinations. There is no network of high-angle boundaries as observed for the terraced sample in Figure 7c. Furthermore, additional substructure is again observed in the backbone derivative map in Figure 8c with a change in angle <15° per pixel. These features indicate that within the large quasi-domains of the isotropic nanoribbon sample the direction of the backbone angle does not change smoothly but rather abruptly. Changes in the backbone orientation are therefore promoted throughout the terraced layers by the side chain interdigitation, which is in agreement with the picture obtained for the terraced morphology with lower order in Figure 7. The features are also of similar size as the quasi-domains of the terraced morphology and of the same width (~80 nm) as the high-angle domain boundaries in Figure 7c. This may be related to a maximum size that the quasi-domains with perfectly parallel backbones can obtain within the isotropic nanoribbon morphology.

After annealing and cooling into the isotropic nanoribbon morphology, the average percentage order shown in Figure 8f is increased to $57 \pm 4\%$. From this map, it can be seen that the areas with largest degrees of order are found where the backbone direction is constant over larger areas and reduced at sites of half integer disclinations. This observation indicates that the increased average degree of order is related to a more homogeneous backbone orientation within the quasi-domains. Similar to the terraced PBTTT sample, the average degree of order of the isotropic sample is largely independent of the different input parameters (see Supporting Information).

A quite drastic change is observed for the tilt angle for the isotropic nanoribbon sample. The tilt angle distribution shown in Figure 8e is narrower compared to the terraced sample in Figure 7d with the average tilt angle of the distribution around $45 \pm 5°$. This is a much stronger tilted backbone compared to the 65° tilt observed in the surface NEXAFS and quite unexpected considering that even in the isotropic case the ribbon morphology has a larger degree of order with edge-on backbones within the layers. Similar to the terraced sample, it can be seen that a reduced tilt angle value in Figure 8e is found predominantly at the sites of half integer disclinations, where the degree of order is also low (Figure 8f). However, when considering only pixels with >65% order anywhere in the film, this value is decreased further to only 41°. To our knowledge, no X-ray scattering data exist for isotropic nanoribbon samples to compare with this measured bulk tilt angle. Analogous to the terraced sample discussed above the tilt angle may be influenced by aligned backbones that are not within coherent crystallites. It is likely that these are found at sites of low order such as half integer disclinations and throughout the quasi-domains, where low-angle domain boundaries are present as seen in Figure 8c. Although the apparent discrepancy between surface and bulk orientation could furthermore be influenced by the uncertainties in the input parameters necessary for calculating the bulk tilt angle from STXM, it is possible that surface and bulk have different characteristic tilt angles warranting closer examination in future experiments that exclusively probe the backbone tilt angle in the bulk.

Interesting features are also observed in the STXM measurements of the aligned nanoribbon sample shown in Figure 9. An immediate observation from the backbone orientation map in Figure 9b is that the polymer backbones are not perfectly aligned with the zone-casting direction. Elongated domains with alternating backbone orientation are observed, with orientation deviating by as much as 45° from the casting direction. Close examination of the AFM images (see Figure 9a) and also the higher resolution image in Figure 2f reveals evidence for misalignment of nanoribbons as sketched in the inset of Figure 9a. It has been suggested that the ribbons are formed by stretched polymer backbones due to the correlation of the ribbon width with polymer chain length.[21] Using the backbone orientation map in Figure 9b, it is clear that the backbones are always perpendicular to the ribbon orientation but not necessarily parallel to the zone-casting direction. Therefore, even in this highly aligned morphology, we observe quasi-domains of parallel backbones on relatively large length scales. This is in agreement with the surface NEXAFS measurements shown in Figure 4b, where the π^* resonance does not go to zero upon rotation of the polarization parallel to the zone-casting direction at normal X-ray incidence ($\theta = \varphi = 90°$), indicating that a significant proportion of
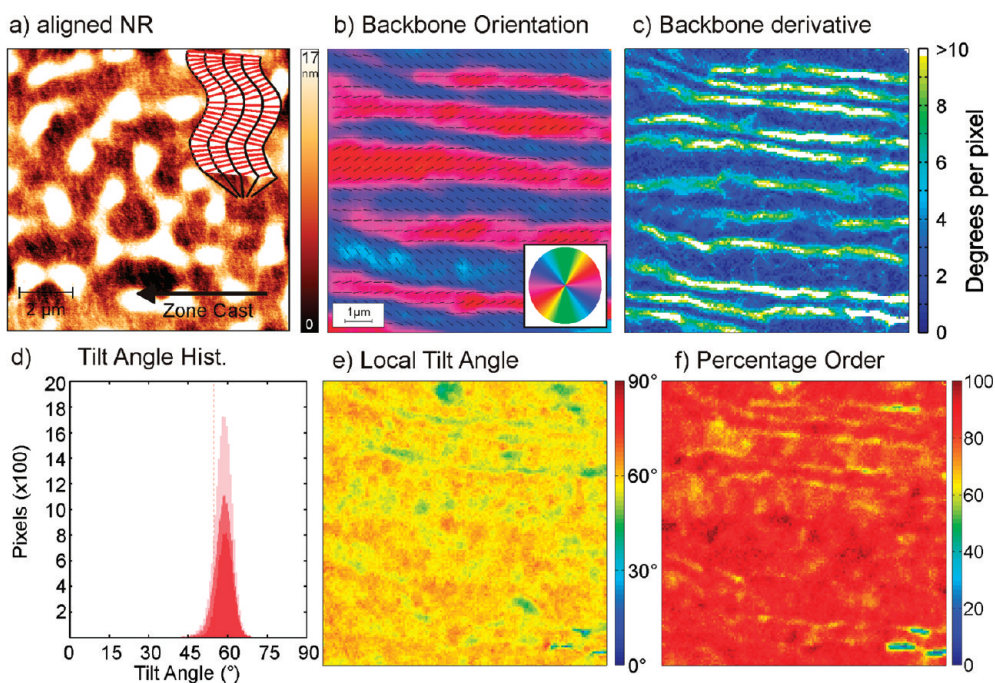
Figure 9. (a) AFM image of aligned nanoribbon PBTTT on mica substrate before floating off for X-ray transmission measurements. The inset shows a magnified drawing of the ribbon orientation (black) and backbone directions (red). (b) Backbone orientation maps calculated from multiple STXM images taken of the same spot of the film but with different incident linear polarization of the X-ray beam, (c) rate of change of the backbone orientation. (e) Calculated local tilt angle and (f) the degree of order map. The histogram in (d) shows the distribution of tilt angles for all pixels (light red) and for >59, >77, and >86% order.

the polymer chains are not parallel to the zone-casting direction.

The backbone derivative map in Figure 9c has been rescaled, as no high-angle domain boundaries (>25° per pixel) are observed. The rescaled image features domain boundaries with a maximum of ~10° change of the backbone orientation per pixel. However, it can be seen that the domain boundaries extend up to five pixels (375 nm) in width (with <150 nm resolution). Integrated over this width, the change in backbone orientation can be more than the 25° defining high-angle domain boundaries. High-angle domain boundaries are therefore present in aligned nanoribbons but extend over relatively larger areas. This observation can be directly correlated with a reduction in the degree of order along these domain boundaries in the degree of order map in Figure 9f. Again, the reduced degree of order can be either due to an increased amorphous fraction or due to misalignment of the backbones within the individual pixels. The average degree of order of the aligned nanoribbon morphology is measured to be 83 ± 1%, significantly higher than that measured for the isotropic nanoribbon sample linking the backbone alignment with a larger degree of order. A significant number of pixels have close to 100% order, which would indicate perfectly aligned polymer backbones throughout the bulk of the film and within the resolved area.

The large degree of order in the aligned nanoribbon sample is also reflected in the calculated tilt angles. A distribution of tilt angles with an average of 58 ± 5° is observed when including all pixels and increasing to 63° when including only pixels with >95% order as shown in the histogram in Figure 9d. This is in good agreement with the measured tilt angles at the sample surface between 64 and 67° as described above, indicating that the backbones are edge-on throughout the film and that there is excellent interlayer registration of the backbone orientation. It is interesting to note that the broad quasi-domain boundaries with relatively lower degree of order only slightly influence the average tilt angle within the bulk of the film. The fact that good agreement is observed between the surface and bulk tilt angle for this sample suggests that for the isotropic nanoribbon film the lower calculated bulk tilt angle is indicative of real differences in the surface and bulk orientations introduced by the fractions with lower degree of order.

When comparing results of the STXM data analysis for the terraced, isotropic nanoribbon, and aligned nanoribbon sample, we can draw the following conclusions. The calculated degree of order increases after annealing from the terraced to the nanoribbon morphology and further increases when aligning the nanoribbons using the zone-casting technique. This is in agreement with our understanding of the calculated percentage order, which is a reflection of the

strength of the dichroism at any given pixel, so that samples with larger change of backbone direction (terraced sample) are expected to have a reduced calculated degree of order compared to samples with aligned backbones (aligned nanoribbon sample). Reduced order is found around the nematic liquid crystal disclination sites and along the high-angle domain boundaries which are observed in the terraced sample. For the aligned nanoribbon sample, excellent agreement of the calculated tilt angle with the surface NEXAFS measurements is observed, indicating that the unit cell structure at the surface prevails all the way through the bulk of the film. The distribution of tilt angles is larger in the terraced and isotropic nanoribbon sample, and the lower average values may be caused by oriented backbones without coherent translational order.

Both the degree of order maps and backbone derivative maps therefore indicated potential sites of charge traps. This has been observed in F8BT due to the strong correlation of high-angle quasi-domain boundaries with the emission maps of light-emitting FETs.[16] It has also been shown using high-resolution scanning Kelvin probe measurements that in isotropic nanoribbon PBTTT films the sites of charge traps are at the edges of the nanoribbons, which cannot be resolved here.[37] The fact that the degree of order in isotropic nanoribbon samples is lower compared to the aligned nanoribbon sample indicates that the change in ribbon orientation may increase the trap density at the edges of ribbons. High-angle domain boundaries can be observed in the terraced and aligned nanoribbon morphology; however, percolation paths may exist around them in both cases.

Large saturation mobility differences have been observed in PBTTT FETs on different substrates. Annealing of the as-cast morphology into the terraced morphology on octyltrichlorosilane (OTS)-treated SiO_x bottom-gate FETs produced large terraces and a greater than 2-fold increase of the saturation mobility, while on bare SiO_x, only small terraces and a lower field-effect mobility were observed.[38] The DF-TEM study discussed above suggested that films with different quasi-domain sizes in bottom-gate FETs showed no differences in their field-effect mobilities, and it was suggested that this may be related to the same density of high-angle domain boundaries in both films.[12] Another study imaged terraced PBTTT using TEM and observed coherent crystallites on a ~10 nm length scale.[26] Next to high-angle domain boundaries, traps may also be present at the edges of coherent crystallites. Analysis of the electrical properties of OTS-SiO_x FETs using the "mobility edge" model allowed the authors to conclude that the trap density is, in fact, similar to the values found in P3HT, indicating that the larger mobility in coherent crystallites rather than the formation of terraces is the origin of the superior performance of

PBTTT. Another publication by the same group also emphasized the importance of grain boundaries in aligned P3HT FETs, where high-angle domain boundaries or boundaries with different backbone tilt pose a significant transport barrier.[28]

Isotropic nanoribbon devices show a similar dependence of the performance on the gate dielectric used as the terraced devices.[27] The saturation mobilities vary from study to study due to the different deposition techniques, but the performance of isotropic nanoribbon FETs does not seem to show a clear improvement over the terraced PBTTT morphology, even though the former morphology has a significantly larger average degree of order of 57% compared to only 35% for the terraced sample and a network of high-angle domain boundaries cannot be resolved in this study. However, the observation of substructure within the quasi-domains in Figure 8c on a length scale of several hundreds of nanometers may indicate that "low-angle" domain boundaries may, in fact, be significant to charge transport due to their increased density in this morphology. The performance of aligned nanoribbon samples in both the polymer backbone and the nanoribbon direction also does not exceed the mobilities observed for the isotropic samples. It has been shown that the degree of paracrystallinity calculated from normalized X-ray diffraction still characterizes this morphology as being close to amorphous.[25] However, the fact that the polymer backbone orientation deviates by as much as 45° from the zone-casting direction indicates that the simple picture of charge transport in the backbone and ribbon direction is not completely accurate. Transport along the zone-casting direction is likely to be influenced also by the defects in the $\pi-\pi$ stacking. Perpendicular to the zone-casting direction, high-angle domain boundaries with reduced order exist, which are likely to act as significant barriers for transport. This study therefore shows that all length scales of ordering need to be considered in order to fully understand the complex microstructures of the different PBTTT morphologies.

CONCLUSION

In conclusion, this paper summarizes a detailed structural characterization of the different PBTTT thin-film morphologies. The surface-sensitive NEXAFS measurements reveal a large dichroism for all morphologies, indicating that pronounced out-of-plane lamella ordering is present even in the as-deposited morphologies despite a lack of evidence for surface ordering in the topography. When rotating zone-cast films around the out-of-plane axis, the NEXAFS spectra at normal incidence exhibit strong dichroism in the π^* absorption, confirming backbone alignment. Combined with optical spectroscopy, the NEXAFS measurements of the zone-cast films give evidence of the ordering

mechanism that aligns the polymer backbones. Zone-casting produces aligned polymer backbones predominately at the surface of the film, with thermal annealing promoting the alignment into the bulk. STXM images of the terraced, isotropic, and aligned nanoribbon morphologies reveal the in-plane backbone orientation of the thin films. The terraced and isotropic nanoribbon films exhibit nematic liquid crystalline order with characteristic half integer disclinations. Maps of the rate of change of backbone angles highlight the presence of high-angle domain boundaries that may serve as deep-trapping sites. The backbone orientation in aligned nanoribbon films shows that the backbone orientation is not necessarily parallel to the zone-casting direction but always perpendicular to orientation of the ribbons, which can divert up to 45° from the zone-casting direction. This observation also explains the nonzero $\pi*$ absorption in surface NEXAFS scans when aligning the E-field polarization parallel to the zone-casting direction. The calculated degree of order and tilt angle maps following our novel data analysis method from the STXM data gives direct evidence of the degree of order evolution for the different samples and highlights that the liquid crystalline disclinations are sites of low order in the film. The characterization of the different PBTTT morphologies in this study highlights the complex microstructure of PBTTT on different length scales that affect charge transport in PBTTT devices.

METHODS

Film Deposition. PBTTT (M_n = 25.6 kg mol^{-1}, M_w = 46.8 kg mol^{-1}, PDI = 1.83) was processed by dissolving in anhydrous 1,2-dichlorobenzne (95% ROMIL). Substrates were cleaned in a sonic bath with acetone and 2-propanol before treatment in an oxygen plasma for 10 min. Films of around 30 nm thickness were prepared by spin-coating from a 10 g/L solution at 2000 rpm for 90 s. Aligned PBTTT films were produced by zone-casting, where the solution is slowly deposited on a substrate and directionally dried as the droplet is moved along the substrate.[22] Around 70 nm thick films were prepared as reported previously by casting from a solution of 2 g/L PBTTT in anhydrous 1,2-dichlorobenzene (95% ROMIL).[27] Both the solution and the substrate were held at constant temperatures of 140 and 100 °C, respectively, during the deposition. The substrate was moved underneath the nozzle at ~30 μm s^{-1} while depositing the solution in nitrogen atmosphere. The aligned nanoribbon films were obtained by placing the zone-cast films onto a hot plate at 275 °C for a few seconds and slowly cooling to room temperature in a nitrogen-filled glovebox.

NEXAFS Spectroscopy. Surface NEXAFS spectra at the carbon edge were recorded with varying X-ray angles of incidence at the Soft X-ray Spectroscopy Beamline at the Australian Synchrotron, Victoria, Australia.[39] Nearly perfectly linearly polarized photons ($P \approx 1$) from an undulator X-ray source with high spectral resolution of $E/\Delta E \leq 10\,000$ are focused into an ultrahigh vacuum chamber on ~0.4 × 1 mm sample area. The TEY signal of all photoelectrons ejected from the sample surface was measured by recording the drain current flowing from the sample. The limited escape depth of the photoelectrons from within polymer films makes TEY NEXAFS surface-sensitive. Measurements on poly(3-hexylthiophene) (P3HT) films determined the probing depth to be around 2.5 nm.[32] The previously described "stable monitor method" was employed to normalize the recorded signal intensities.[33] The incident photon flux is measured using a gold mesh placed in the X-ray beam in front of the sample for signal normalization. Prior to sample measurements a clean sputtered gold specimen is measured in order to determine the carbon contamination on the gold mesh, and this contamination is assumed to be stable throughout the following measurements. The normalized spectra were scaled by subtracting a background which scales according to the atomic scattering factors of the material prior to the onset of the first feature setting (A(280 eV)) and dividing by A(320 eV). The peaks' intensities in the spectra give information about the orientation of the transition dipole moments (TDM) with respect to the plane of the substrate. For carbon ring systems, it has been shown that 1s (C=C) → $\pi*$ TDMs are oriented perpendicular to the ring plane.[31] For PBTTT, the 1s → $\pi*$ TDMs therefore are perpendicular to the plane of the thienothiophene and thiophene rings, while the 1s (C−C) → $\sigma*$ TDMs are oriented parallel to these bonds, which are predominantly found in the tetradecyl side chains.[24,31] All transitions are localized on the carbon atom of the excited electron due to the localized nature of the C1s orbital. For a sample with threefold or higher symmetry and nearly perfectly linearly polarized X-rays, the dependence of the transition intensity I on the tilt angle γ between the TDM and the substrate and X-ray angle of incidence, θ is given by[31]

$$I = \frac{1}{3}\left[1 + \frac{1}{2}(3\cos^2\theta - 1)(3\cos^2\gamma - 1)\right] \quad (2)$$

For a sample with two-fold rotational symmetry, such as an aligned polymer film found in the zone-cast PBTTT samples, the relationship is altered to[31]

$$I = \cos^2\gamma\,\cos^2\theta + \sin^2\gamma\,\sin^2\theta\,\cos^2\varphi \quad (3)$$

where φ is the angle between the in-plane component of the X-ray electric field vector and the alignment direction of the film. However, it is important to realize that for both equations values for the tilt angle γ exist for which the predicted intensity is independent of θ. A tilt angle of γ = 54.7° (magic angle) in eq 2 or γ = 45° (φ = 0°) in eq 3 could represent an amorphous film with random orientation of the TDMs or a film with a tilt angle at that particular value of γ. Only when extracting tilt angles close to 0 or 90° can a narrow distribution of the molecular orientation be unambiguously inferred. No beam damage was observed when repeatedly recording spectra in the same spot, and this possibility was further reduced by moving to a fresh sample area for every spectrum measured. Both the spectral normalization and the peak fitting for tilt angle extraction were performed with the Whooshka software package developed by Benjamin Watts.

Scanning Transmission X-ray Microscopy. STXM measurements were performed at the PolLux beamline at the Swiss Light Source, Paul Scherrer Institut, Villigen, Switzerland.[40,41] The transmitted X-ray intensity through a sample in an evacuated chamber was recorded using a scintillator and photomultiplier tube. The details of the analysis used here closely follow that described by Watts et al.[16] but with a small change in the molecular model, as briefly outlined below.

The signal was converted to an X-ray optical density OD = ln(I_0/I) by comparing the signal to the X-ray intensity I_0 without the sample in place. Spectra were recorded as a function of energy between 280 and 320 eV with a resolution of 0.1 eV. STXM images were recorded by mapping the OD as a function of position with X-ray focus better than 25 nm diameter and X−Y sample position resolution better than 1 nm. For the

terraced and isotropic nanoribbon samples, the pixel size was 35 and 40 nm, respectively. However, each pixel was averaged with its nearest neighbors in order to reduce noise, therefore reducing the resolution to 70 and 80 nm, respectively. This was not necessary for the aligned nanoribbon sample, where the pixel size was 75 nm. For measurements allowing computation of domain orientation and molecular order, a rotation stage was used to rotate the sample with respect to the fixed linear polarization of the synchrotron. We estimate that the alignment of the images is possible within 1 pixel offset from each other, therefore giving an upper limit to the resolution of twice the pixel size. Four images were acquired of the same region of the sample at orientations of 0, 45, 90, and 135° with respect to the X-ray polarization. The film thickness was normalized by dividing the polarization-dependent images by the image at 320 eV, which only shows thickness modulations (OD(285.6 eV)/OD(320 eV)).

To calculate the backbone orientation map, the thickness-normalized OD maps were fitted at each sample position using the $\cos^2$ relationship on the angle of the incoming (in-plane) polarization θ_{ip}:[31]

$$OD = M[P\cos^2(\beta + \theta_{ip}) + (1 - P)\sin^2(\beta + \theta_{ip})] + C \quad (4)$$

The fitting parameter β directly represents the average orientation of the TDMs probed at this particular sample position (see inset of Figure 1a). $P = 0.89$ is the Stöhr polarization value of the incident X-ray beam at PolLux, and M represents the in-plane magnitude of the directed resonance intensity oriented at angle β, whereas the constant resonance intensity, C, is observed at all angles. The parameters M and C can furthermore be used to derive the local degree of order and the out of plane tilt angle, γ.

Because the STXM operates at normal X-ray incidence, the measurements only probe the in-plane components of the TDMs at each pixel. Therefore, in order to calculate the three-dimensional orientation of the molecules, we must first elucidate the out-of-plane vector components of the TDM. This is possible because the total resonance intensity (TRI), which is the absorption intensity of the TDMs at any given pixel integrated over all incoming X-ray directions, must be constant for the thickness-normalized OD maps of a given material. Once the TRI for the NEXAFS resonance is known, the unobserved out-of-plane intensity is simply the difference between the TRI and the measured in-plane intensities. The previous 3D orientation analysis of F8BT[16] utilized two assumptions to evaluate the TRI for the π^* resonance of that material. First, the constant in-plane resonance intensity, C, was assumed to represent three-dimensionally amorphous material and therefore indicates an equal, unobserved out-of-plane resonance intensity corresponding to the same amorphous fraction of the material. This leaves the out-of-plane resonance intensity component corresponding to the aligned fraction of molecules as the only unobserved quantity and thus the observed summed resonance intensity (T) is given by

$$T = M + 3C \quad (5)$$

The second assumption made was that the sample film had enough variation in conformations present that the unobserved resonance intensity corresponding to aligned molecules must be zero in at least one pixel and therefore the TRI must be equal to the largest observed value of T.

Following the above assumptions with the current PBTTT data sets yields a TRI of 3.5 for the terraced and isotropic nanoribbon samples and a TRI of 2.8 for the aligned nanoribbon. However, the TRI can also be calculated from surface NEXAFS measurements at the magic angle of X-ray incidence. At the magic X-ray angle of incidence of 54.7°, eq 2 yields $I = 1/3$TRI for any given tilt angle. Therefore, we can deduce the TRI from the surface NEXAFS scans of the isotropic samples (see Supporting Information) and find an average TRI value of 2.4 from these measurements. The TRI values obtained by these two methods are in stark disagreement and require reconsidering the appropriateness of the assumptions made in the previous F8BT analysis for the PBTTT system considered here.

First, the known layered structure of PBTTT[4,19] means that the observed in-plane constant resonance intensity would very likely correspond to variations in molecular orientation within a resolved pixel and possible between self-ordered vertical layers rather than to three-dimensionally amorphous material. Second, PBTTT is a highly crystalline material with self-ordered layers and a unit cell with a certain backbone tilt, and so the assumption of zero out-of-plane intensity in at least one pixel is far less likely to hold true. Further, the PBTTT STXM data do not display the range of values that was observed in the F8BT measurements, underscoring the unlikelihood of a particular conformation existing within the measured sample area. However, if we define T by considering only an in-plane contribution of the amorphous TDMs

$$T = M + 2C \quad (6)$$

with M and C as fitted in eq 4, then the maximum observed value of T can be seen as a lower limit for the TRI. Also, since PBTTT is known to preferentially orient strongly edge-on and therefore with the π^* resonance mostly in-plane (as seen in the crystal cell structure[19] as well as the TEY NEXAFS analysis presented in Table 1), the out-of-plane resonance intensity is expected to be small and the TRI is expected to be close to the lower limit given by T.

From histograms of T (see Supporting Information), TRI lower limits of 2.4, 2.4, and 2.2 are deduced for the terraced, isotropic nanoribbon, and aligned nanoribbon samples, respectively. These values agree closely with the TRI estimate derived from the magic angle NEXAFS spectra, and therefore, a TRI of 2.4 was chosen for PBTTT and eq 6 used for the analysis of the STXM data presented in this article. As discussed in the previous 3D orientation analysis of F8BT,[16] the features in the calculated maps of molecular orientation and order are not strongly dependent on the precise choice of TRI. However, the average values are somewhat dependent on the TRI choice, and the induced errors are presented in the Supporting Information.

With knowledge of TRI, the unobserved resonance intensity of the ordered polymer can be estimated by subtracting the observed summed resonance intensity from the TRI, resulting in the total length of the ordered, directed TDM, D:

$$|D| = \text{TRI} - 2C \quad (7)$$

Knowledge of $|D|$ at each point of the sample opens up the possibility to fully characterize the ordered, directed TDM vector, such as the degree of order by evaluating its contribution to the TRI:

$$\text{order} = \frac{|D|}{\text{TRI}} \times 100\% \quad (8)$$

as well as the local out of plane tilt angle γ through comparison of its vector components:

$$\gamma = \sin^{-1}\left[\sqrt{\frac{M}{|D|}}\right] \quad (9)$$

The maps of these material properties are discussed in the paper above.

Organic Field-Effect Transistors. Interdigitated gold source and drain electrodes were patterned onto 1737F alkali-free glass (Präzisions Glas and Optik GmbH) followed by vacuum evaporation of a 20 nm thick gold layer with an underlying 1 nm chromium adhesion layer. The channel length $L = 40$ μm and width of $W = 26$ mm provided long channel lengths to minimize contact effects. PBTTT films were deposited via zone-casting as described above both perpendicular and parallel to the current direction. A 450 nm thick poly(methyl methacrylate) (PMMA) film deposited via spin-coating served as the gate dielectric in this top-gate, bottom contact architecture. A gold gate electrode was subsequently deposited by evaporation through a shadow mask. The current (I_d)−gate voltage (V_g) characteristics of the finished devices at a source−drain voltage $V_{DS} = -60$ V were measured using an Agilent 4155B semiconductor parameter analyzer. The capacitance per unit area C_i was measured

with grounded electrodes, and the saturation mobilities μ and threshold voltages V_T can be calculated from the gradual channel approximation:[42]

$$I = \frac{W}{2L}\mu C_i(V_g - V_T)^2 \qquad (10)$$

Conflict of Interest: The authors declare no competing financial interest.

Supporting Information Available: Fits of NEXAFS spectra to Gaussian oscillators and step-edge; full set of angle-dependent NEXAFS spectra of the aligned nanoribbon sample; raw STXM images; histograms of the observed summed resonance intensity; comparison of NEXAFS spectra of the different morphologies at 55° about 285 eV used to estimate the TRI; investigation of the sensitivity STXM analysis to the TRI used and the disorder model used. This material is available free of charge *via* the Internet at http://pubs.acs.org.

REFERENCES AND NOTES

1. Sirringhaus, H.; Bird, M.; Richards, T.; Zhao, N. Charge Transport Physics of Conjugated Polymer Field-Effect Transistors. *Adv. Mater.* **2010**, *22*, 3893–3898.
2. Gelinck, G.; Heremans, P.; Nomoto, K.; Anthopoulos, T. D. Organic Transistors in Optical Displays and Microelectronic Applications. *Adv. Mater.* **2010**, *22*, 3778–3798.
3. Sirringhaus, H.; Brown, P. J.; Friend, R. H.; Nielsen, M. M.; Bechgaard, K.; Langeveld-Voss, B. M. W.; Spiering, A. J. H.; Janssen, R. A. J.; Meijer, E. W.; Herwig, P.; *et al.* Two-Dimensional Charge Transport in Self-Organized, High-Mobility Conjugated Polymers. *Nature* **1999**, *401*, 685–688.
4. McCulloch, I.; Heeney, M.; Bailey, C.; Genevicius, K.; Mac-Donald, I.; Shkunov, M.; Sparrowe, D.; Tierney, S.; Wagner, R.; Zhang, W.; *et al.* Liquid-Crystalline Semiconducting Polymers with High Charge-Carrier Mobility. *Nat. Mater.* **2006**, *5*, 328–333.
5. DeLongchamp, D. M.; Kline, R. J.; Fischer, D. A.; Richter, L. J.; Toney, M. F. Molecular Characterization of Organic Electronic Films. *Adv. Mater.* **2011**, *23*, 319–337.
6. Salleo, A.; Kline, R. J.; DeLongchamp, D. M.; Chabinyc, M. L. Microstructural Characterization and Charge Transport in Thin Films of Conjugated Polymers. *Adv. Mater.* **2010**, *22*, 3812–3838.
7. Rivnay, J.; Jimison, L. H.; Northrup, J. E.; Toney, M. F.; Noriega, R.; Lu, S. F.; Marks, T. J.; Facchetti, A.; Salleo, A. Large Modulation of Carrier Transport by Grain-Boundary Molecular Packing and Microstructure in Organic Thin Films. *Nat. Mater.* **2009**, *8*, 952–958.
8. McNeill, C. R. Imaging the Domain Structure of Organic Semiconductor Films. *J. Polym. Sci., Part B: Polym. Phys.* **2011**, *49*, 909–919.
9. Kalihari, V.; Tadmor, E. B.; Haugstad, G.; Frisbie, C. D. Grain Orientation Mapping of Polycrystalline Organic Semiconductor Films by Transverse Shear Microscopy. *Adv. Mater.* **2008**, *20*, 4033–4039.
10. Zhang, J.; Rabe, J. P.; Koch, N. Grain-Boundary Evolution in a Pentacene Monolayer. *Adv. Mater.* **2008**, *20*, 3254–3257.
11. Brinkmann, M.; Contal, C.; Kayunkid, N.; Djuric, T.; Resel, R. Highly Oriented and Nanotextured Films of Regioregular Poly(3-hexylthiophene) Grown by Epitaxy on the Nanostructured Surface of an Aromatic Substrate. *Macromolecules* **2010**, *43*, 7604–7610.
12. Zhang, X.; Hudson, S. D.; DeLongchamp, D. M.; Gundlach, D. J.; Heeney, M.; McCulloch, I. In-Plane Liquid Crystalline Texture of High-Performance Thienothiophene Copolymer Thin Films. *Adv. Funct. Mater.* **2010**, *20*, 4098–4106.
13. Kuehn, S.; Pingel, P.; Breusing, M.; Fischer, T.; Stumpe, J.; Neher, D.; Elsaesser, T. High-Resolution Near-Field Optical Investigation of Crystalline Domains in Oligomeric PQT-12 Thin Films. *Adv. Funct. Mater.* **2011**, *21*, 860–868.
14. Bräuer, B.; Virkar, A.; Mannsfeld, S. C. B.; Bernstein, D. P.; Kukreja, R.; Chou, K. W.; Tyliszczak, T.; Bao, Z.; Acremann, Y. X-ray Microscopy Imaging of the Grain Orientation in a Pentacene Field-Effect Transistor. *Chem. Mater.* **2010**, *22*, 3693–3697.
15. Hub, C.; Burkhardt, M.; Halik, M.; Tzvetkov, G.; Fink, R. *In Situ* STXM Investigations of Pentacene-Based OFETs during Operation. *J. Mater. Chem.* **2010**, *20*, 4884–4887.
16. Watts, B.; Schuettfort, T.; McNeill, C. R. Mapping of Domain Orientation and Molecular Order in Polycrystalline Semiconducting Polymer Films with Soft X-ray Microscopy. *Adv. Funct. Mater.* **2011**, *21*, 1122–1131.
17. Kowarik, S.; Broch, K.; Hinderhofer, A.; Schwartzberg, A.; Oriol, O. J.; Kilcoyne, D.; Schreiber, F.; Leone, S. R. Crystal Grain Orientation in Organic Homo- and Heteroepitaxy of Pentacene and Perfluoropentacene Studied with X-ray Spectromicroscopy. *J. Phys. Chem. C* **2010**, *114*, 13061–13067.
18. McCulloch, I.; Heeney, M.; Chabinyc, M. L.; DeLongchamp, D.; Kline, R. J.; Coelle, M.; Duffy, W.; Fischer, D.; Gundlach, D.; Hamadani, B.; *et al.* Semiconducting Thienothiophene Copolymers: Design, Synthesis, Morphology, and Performance in Thin-Film Organic Transistors. *Adv. Mater.* **2009**, *21*, 1091–1109.
19. Chabinyc, M. L.; Toney, M. F.; Kline, R. J.; McCulloch, I.; Heeney, M. X-ray Scattering Study of Thin Films of Poly-(2,5-bis(3-alkylthiophen-2-yl)thieno[3,2-*b*]thiophene. *J. Am. Chem. Soc.* **2007**, *129*, 3226–3237.
20. DeLongchamp, D. M.; Kline, R. J.; Jung, Y.; Lin, E. K.; Fischer, D. A.; Gundlach, D. J.; Cotts, S. K.; Moad, A. J.; Richter, L. J.; Toney, M. F.; *et al.* Molecular Basis of Mesophase Ordering in a Thiophene-Based Copolymer. *Macromolecules* **2008**, *41*, 5709–5715.
21. DeLongchamp, D. M.; Kline, R. J.; Jung, Y.; Germack, D. S.; Lin, E. K.; Moad, A. J.; Richter, L. J.; Toney, M. F.; Heeney, M.; McCulloch, I. Controlling the Orientation of Terraced Nanoscale "Ribbons" of a Poly(thiophene) Semiconductor. *ACS Nano* **2009**, *3*, 780–787.
22. Tang, C. B.; Tracz, A.; Kowalewski, T.; Kruk, M.; Zhang, R.; Smilgies, D. M.; Matyjaszewski, K. Long-Range Ordered Thin Films of Block Copolymers Prepared by Zone-Casting and Their Thermal Conversion into Ordered Nanostructured Carbon. *J. Am. Chem. Soc.* **2005**, *1276918*–6919.
23. Brocorens, P.; Van Vooren, A.; Chabinyc, M. L.; Toney, M. F.; Shkunov, M.; Heeney, M.; McCulloch, I.; Cornil, J.; Lazzaroni, R. Solid-State Supramolecular Organization of Polythiophene Chains Containing Thienothiophene Units. *Adv. Mater.* **2009**, *21*, 1193–1198.
24. DeLongchamp, D. M.; Kline, R. J.; Lin, E. K.; Fischer, D. A.; Richter, L. J.; Lucas, L. A.; Heeney, M.; McCulloch, I.; Northrup, J. E. High Carrier Mobility Polythiophene Thin Films: Structure Determination by Experiment and Theory. *Adv. Mater.* **2007**, *19*, 833–837.
25. Rivnay, J.; Noriega, R.; Northrup, J. E.; Kline, R. J.; Toney, M. F.; Salleo, A. Structural Origin of Gap States in Semicrystalline Polymers and the Implications for Charge Transport. *Phys. Rev. B* **2011**, *83*, 121306–121310.
26. Wang, C. C.; Salleo, A.; Jimison, L. H.; Goris, L.; McCulloch, I.; Heeney, M.; Ziegler, A. Microstructural Origin of High Mobility in High-Performance Poly(thieno-thiophene) Thin-Film Transistors. *Adv. Mater.* **2010**, *22*, 697–701.
27. Lee, M. J.; Gupta, D.; Zhao, N.; Heeney, M.; McCulloch, I.; Sirringhaus, H. Anisotropy of Charge Transport in a Uniaxially Aligned and Chain-Extended, High-Mobility, Conjugated Polymer Semiconductor. *Adv. Funct. Mater.* **2011**, *21*, 932–940.
28. Jimison, L. H.; Toney, M. F.; McCulloch, I.; Heeney, M.; Salleo, A. Charge-Transport Anisotropy Due to Grain Boundaries in Directionally Crystallized Thin Films of Regioregular Poly(3-hexylthiophene). *Adv. Mater.* **2009**, *21*, 1568–1572.

29. Hallam, T.; Lee, M.; Zhao, N.; Nandhakumar, I.; Kemerink, M.; Heeney, M.; McCulloch, I.; Sirringhaus, H. Local Charge Trapping in Conjugated Polymers Resolved by Scanning Kelvin Probe Microscopy. *Phys. Rev. Lett.* **2009**, *103*, 256803.

30. DeLongchamp, D. M.; Kline, R. J.; Fischer, D. A.; Lin, E. K.; Richter, L. J.; Chabinyc, M. L.; Toney, M. F.; Heeney, M.; McCulloch, I. Critical Role of Side-Chain Attachment Density on the Order and Device Performance of Polythiophenes. *Macromolecules* **2007**, *40*, 7960–7965.

31. Stöhr, J. NEXAFS Spectroscopy. In *Springer Series in Surface Sciences 25*; Gomer, R., Ed.; Springer: Berlin, 1992; pp 276−285.

32. Chua, L.-L.; Dipankar, M.; Sivaramakrishnan, S.; Gao, X.; Qi, D.; Wee, A. T. S.; Ho, P. K. H. Large Damage Threshold and Small Electron Escape Depth in X-ray Absorption Spectroscopy of a Conjugated Polymer Thin Film. *Langmuir* **2006**, *22*, 8587–8594.

33. Watts, B.; Thomsen, L.; Dastoor, P. C. Methods in Carbon K-Edge NEXAFS: Experiment and Analysis. *J. Electron Spectrosc. Relat. Phenom.* **2006**, *151*, 105–120.

34. McNeill, C. R.; Watts, B.; Thomsen, L.; Ade, H.; Greenham, N. C.; Dastoor, P. C. X-ray Microscopy of Photovoltaic Polyfluorene Blends: Relating Nanomorphology to Device Performance. *Macromolecules* **2007**, *40*, 3263–3270.

35. McNeill, C. R.; Watts, B.; Thomsen, L.; Belcher, W. J.; Kilcoyne, A. L. D.; Greenham, N. C.; Dastoor, P. C. X-ray Spectromicroscopy of Polymer/Fullerene Composites: Quantitative Chemical Mapping. *Small* **2006**, *2*, 1432–1435.

36. Sciascia, C.; Martino, N.; Schuettfort, T.; Watts, B.; Grancini, G.; Antognazza, M. R.; Zavelani-Rossi, M.; McNeill, C. R.; Caironi, M. Sub-Micrometer Charge Modulation Microscopy of a High Mobility Polymeric n-Channel Field-Effect Transistor. *Adv. Mater.* **2011**, *23*, 5086–5090.

37. Hallam, T.; Duffy, C. M.; Minakata, T.; Aando, M.; Sirringhaus, H. A Scanning Kelvin Probe Study of Charge Trapping in Zone-Cast Pentacene Thin Film Transistors. *Nanotechnology* **2009**, *20*, 025203–025211.

38. Kline, R. J.; DeLongchamp, D. M.; Fischer, D. A.; Lin, E. K.; Heeney, M.; McCulloch, I.; Toney, M. F. Significant Dependence of Morphology and Charge Carrier Mobility on Substrate Surface Chemistry in High Performance Polythiophene Semiconductor Films. *Appl. Phys. Lett.* **2007**, *90*, 062117.

39. Cowie, B. C. C.; Tadich, A.; Thomsen, L. The Current Performance of the Wide Range (90−2500 eV) Soft X-ray Beamline at the Australian Synchrotron. *AIP Conf. Proc.* **2010**, *1234*, 307–310.

40. Flechsig, U.; Quitmann, C.; Raabe, J.; Booge, M.; Fink, R.; Ade, H. The PolLux Microspectroscopy Beamline at the Swiss Light Source. *AIP Conf. Proc.* **2007**, *879*, 505–508.

41. Raabe, J.; Tzvetkov, G.; Flechsig, U.; Boge, M.; Jaggi, A.; Sarafimov, B.; Vernooij, M. G. C.; Huthwelker, T.; Ade, H.; Kilcoyne, D.; *et al.* PolLux: A New Facility for soft X-ray Spectromicroscopy at the Swiss Light Source. *Rev. Sci. Instrum.* **2008**, *79*, 113704.

42. Horowitz, G. Organic Field-Effect Transistors. *Adv. Mater.* **1998**, *10*, 365–377.